

## Article

# Structure, Electrochemical, and Transport Properties of Li- and F-Modified P2-Na<sub>2/3</sub>Ni<sub>1/3</sub>Mn<sub>2/3</sub>O<sub>2</sub> Cathode Materials for Na-Ion Batteries

Xinglong Chen, Wenyue Guo, Rui Li, Peng Du, Xiaowen Zhan \*  and Shan Gao \*

Anhui Province Key Laboratory of Chemistry for Inorganic/Organic Hybrid Functionalized Materials, Key Laboratory of Structure and Functional Regulation of Hybrid Materials of Ministry of Education, School of Chemistry and Chemical Engineering, School of Materials Science and Engineering, Anhui University, Hefei 230601, China

\* Correspondence: xiaowen.zhan@ahu.edu.cn (X.Z.); shangao@ahu.edu.cn (S.G.)

**Abstract:** The development of cobalt-free P2-Na<sub>2/3</sub>Ni<sub>1/3</sub>Mn<sub>2/3</sub>O<sub>2</sub> cathodes is hampered by poor electrochemical performance, resulting from structural instability during high-voltage cycling. Herein, Li<sup>+</sup> and F<sup>-</sup> ions are introduced simultaneously via a simple sol-gel method. The F not only enters the lattice but forms chemically stable NaF on the surface. The modified electrode delivered significantly better electrochemical performance than the pristine one, including much-enhanced capacity retention (64% vs. 36%, 100 cycles) at 0.5 C and a four-time higher capacity output at 10 C. The ex situ XRD and in situ Raman analysis revealed cyclability enhancement mechanisms in terms of inhibiting the P2-O2 phase transition and Na<sup>+</sup>/vacancy ordering. The conductivity measurements (based on AC impedance and DC polarization) and GITT analysis proved, on both bulk material and electrode levels, that Na<sup>+</sup> conduction and, thus, rate performance is notably promoted by doping. The individual contribution of Li and F to the overall performance improvement was also discussed. Furthermore, a solid-state sodium-metal battery was successfully demonstrated with the modified cathode. The above results verify that Li<sup>+</sup>/F<sup>-</sup> incorporation can enable enhancements in both cyclability and rate capability of the P2-Na<sub>2/3</sub>Ni<sub>1/3</sub>Mn<sub>2/3</sub>O<sub>2</sub> cathodes and are expected to provide a new perspective for the rational design of high-performance layered oxide cathode materials for progressive sodium-ion batteries.

**Keywords:** sodium-ion battery; P2-type layered transition-metal oxide; structural stability; solid-state sodium-metal batteries



**Citation:** Chen, X.; Guo, W.; Li, R.; Du, P.; Zhan, X.; Gao, S. Structure, Electrochemical, and Transport Properties of Li- and F-Modified P2-Na<sub>2/3</sub>Ni<sub>1/3</sub>Mn<sub>2/3</sub>O<sub>2</sub> Cathode Materials for Na-Ion Batteries.

*Coatings* **2023**, *13*, 626. <https://doi.org/10.3390/coatings13030626>

Academic Editors: Alexander Modestov and Je Moon Yun

Received: 20 February 2023

Revised: 7 March 2023

Accepted: 14 March 2023

Published: 16 March 2023



**Copyright:** © 2023 by the authors. Licensee MDPI, Basel, Switzerland. This article is an open access article distributed under the terms and conditions of the Creative Commons Attribution (CC BY) license (<https://creativecommons.org/licenses/by/4.0/>).

## 1. Introduction

Commercialized in 1991 by SONY, rechargeable lithium-ion batteries (LIBs) featuring high energy density have dominated consumer electronics and emerged as the technology of choice for powering electric vehicles [1,2]. However, they still suffer from limited Li reserves and high costs of raw materials, arousing questions about their long-term supply stability and encouraging the research and development of various “beyond Li-ion” batteries [3]. In particular, sodium-ion batteries (SIBs) with higher materials abundance and a lower cost (compared to LIBs) have been widely considered for large-scale grid storage applications [4,5]. Owing to their similar battery components and electrochemical energy storage mechanism, most of the current knowledge on LIBs can be directly applied to SIBs, making SIBs, among all other beyond-Li battery systems, the most realistic alternative to LIBs [6].

In SIBs, the cathode material determines the energy density and manufacturing cost of the battery [7]. Thus far, many cathode materials (i.e., layered compounds, polyanions, Prussian blue, organic materials, etc.) have been proposed, with major efforts parted between the Na-based polyanions and layered transition-metal oxides (NaTMO<sub>2</sub>, TM=Mn,

Co, Ni, and Fe, etc.) [8]. The NaTMO<sub>2</sub> family mainly comprises prismatic (P2) and octahedral (O3) phases, which are named according to the coordination environment of Na (prismatic or octahedral) and the number of transition-metal oxide layers (TMO<sub>2</sub>) in the unit cell [9,10]. Troubled by the complicated phase transitions occurring during the charge/discharge and irreversible structural changes, both phases exhibit low reversible capacity, fast capacity decay, and a short cycle life [11,12]. Despite this, P2 compounds are attracting more attention, owing to their better rate performance stemming from the fast two-dimensional Na<sup>+</sup> transport channels in their crystal structure [13]. Particularly, P2-type Na<sub>2/3</sub>Ni<sub>1/3</sub>Mn<sub>2/3</sub>O<sub>2</sub> (hereinafter named NNMO), first synthesized by Dahn et al., can deliver about 170 mAh g<sup>-1</sup>, enabled by the Ni<sup>2+</sup>/Ni<sup>4+</sup> redox couple in the range of 2.0–4.5 V and is stable in the air [14]. Meanwhile, the cobalt-free composition of NNMO is beneficial for practical applications due to the global trend to reduce cobalt that is toxic, high-cost and limited in supply [15,16]. Unfortunately, the unavoidable P2–O2 phase transition at high voltages and Na<sup>+</sup>/vacancy ordering can lead to structure degradation, eventually causing unsatisfying cycling and rate performance [17,18]. In order to tackle these issues, existing strategies mainly include bulk doping, [14,19–23] surface coating, [24–27] and morphology tuning [28]. Among them, element doping has been frequently explored because of its high efficiency and potentially good scalability. For example, partial Ti substitution for Mn with compatible ionic radii but very different Fermi energy levels led to a P2 material with fully disordered Na<sup>+</sup>/vacancy distribution, significantly promoting the rate's performance and cycling stability of NNMO (83.9% capacity retention after 500 cycles at 1 C) [29]. A recent work by Xiao et al. demonstrated that by Li doping in P2-structured Na<sub>0.66</sub>Ni<sub>0.25</sub>Mn<sub>0.75</sub>O<sub>2</sub>, not only is the harmful P2–O2 transition inhibited, but the oxygen and Mn redox reactivities can be suppressed, leading to a promotion of the Ni redox [30]. Other cations, such as Fe<sup>3+</sup>, Al<sup>3+</sup>, Zn<sup>2+</sup> and Mg<sup>2+</sup>, have also been shown to inhibit the harmful P2–O2 phase transition, thereby improving the cycling performance [31]. Alternatively, anion doping, i.e., the substitution of O<sup>2-</sup> by F<sup>-</sup>, was proved effective in inducing a partial reduction of Mn<sup>4+</sup> to Mn<sup>3+</sup> and forming a more stable TM–F bond (compared to TM–O), thereby stabilizing the structure during cycling [32]. Furthermore, F<sup>-</sup> doping can reduce the Ni<sup>2+</sup>/Ni<sup>3+</sup> ratio as a result of charge compensation, leading to a higher capacity and rate capability [33]. Although individual cation or anion doping has been well studied, the synergistic effects of cation/anion co-doping are much less explored [34,35]. Given the different enhancement mechanisms discussed above, the interplay of anion/cation dopants may create new opportunities towards the rational design of P2-type NaTMO<sub>2</sub> cathode materials.

Herein, we successfully prepared Li<sup>+</sup>/F<sup>-</sup> co-doped Na<sub>2/3</sub>Li<sub>0.1</sub>(Ni<sub>1/3</sub>Mn<sub>2/3</sub>)<sub>0.9</sub>O<sub>1.95</sub>F<sub>0.05</sub> (hereinafter named NLNMOF) compounds and analyzed their structural and electrochemical properties as cathode materials for SIBs. Our results show that NLNMOF has better air stability and exhibits much-enhanced cycling and rate performance than the undoped one. The ex situ XRD and in situ Raman results reveal the beneficial effect of Li<sup>+</sup>/F<sup>-</sup> modification in terms of suppressing the P2–O2 phase transition and inducing Na<sup>+</sup>/vacancy ordering. The conductivity measurements and GITT analysis suggested that the more favorable interfacial kinetics and faster solid-state Na<sup>+</sup> diffusivity are responsible for the rate's improvement. The present work demonstrates Li<sup>+</sup>/F<sup>-</sup> co-doping as an effective strategy for stabilizing NNMO cathodes for progressive SIBs.

## 2. Experimental Section

### 2.1. Materials Synthesis

The Li<sup>+</sup>/F<sup>-</sup>-modified NLNMOF samples were synthesized via a sol–gel method. Specifically, stoichiometric amounts of NaNO<sub>3</sub> (Aladdin, 99.7%), NiNO<sub>3</sub>·6H<sub>2</sub>O (Aladdin, 98%), Mn(NO<sub>3</sub>)<sub>2</sub>·4H<sub>2</sub>O (Aladdin, 98%), and LiNO<sub>3</sub> (Aladdin, 99.9%) were dissolved in 40 mL of deionized water. A proper amount of C<sub>6</sub>H<sub>8</sub>O<sub>7</sub>·H<sub>2</sub>O (Aladdin, 99.5%) and NaF (Aladdin, 99.99%) were added successively with an interval of 15 min. The molar ratio of C<sub>6</sub>H<sub>8</sub>O<sub>7</sub>·H<sub>2</sub>O to the transition-metal ions is 1:1. It should be noted that the Na element

contribution from NaF was excluded when calculating the mole number of  $\text{NaNO}_3$ , for which a 5% Na excess was added to compensate the Na loss during high-temperature annealing. Subsequently, a gel was obtained after stirring the solution at  $80\text{ }^\circ\text{C}$  for 12 h, which was dried thoroughly at  $150\text{ }^\circ\text{C}$  for 12 h and ground to obtain the precursor powders. Finally, the powders were annealed in air at  $450\text{ }^\circ\text{C}$  for 6 h, followed by  $950\text{ }^\circ\text{C}$  for 15 h, with a ramp rate of  $5\text{ }^\circ\text{C min}^{-1}$ . The preparation of NNMO followed the same method, except that no NaF and  $\text{LiNO}_3$  were used. Detailed recipes for preparing NNMO and NLNMOF samples are listed in Table S1. In order to prepare the pellet samples for conductivity measurements, NNMO or NLNMOF powder was simply ground and pressed into pellets with a diameter of 12 mm and a thickness of 1 mm (8 metric tons, YLJ-15T-LD, MTI Corp., Hefei, China), which were further densified using a cold isostatic press (200 MPa, YLJ-CIP-15, MTI Corp., Hefei, China). Finally, the ceramics were sintered at  $1000\text{ }^\circ\text{C}$  for 8 h in the air.

### 2.2. Structure and Composition Characterization

X-ray diffraction (XRD) patterns were gathered with a Rigaku X-ray diffractometer (Rigaku, Tokyo, Japan) at 40 kV and 100 mA under  $\text{Cu K}\alpha$  radiation ( $\lambda = 0.154\text{ nm}$ ). The XRD refinement was performed using the Rietveld method with GSAS. Field emission scanning electron microscopy (SEM, Hitachi S-4800, 20 kV, Tokyo, Japan) and energy dispersive spectroscopy (EDS) were used to observe the morphology and element distribution. The surface valence states were analyzed by X-ray photoelectron spectroscopy (XPS, Thermo Scientific™ K-Alpha™+ spectrometer, Waltham, MA, USA), with the peak fitting conducted using Casa XPS. All spectral lines have been calibrated based on the C 1s peak at 284.8 eV. Raman spectra were acquired using a Via-reflex Raman spectrometer (HORIBA XploRA PLUS, Kyoto, Japan) utilizing a 638 nm laser with a laser intensity of 10% and an acquisition time of 30 s. All spectra were recorded twice to strengthen the signal-to-noise ratio. The in situ Raman analysis was carried out using an in situ Raman cell (Beijing Scistar Technology Co., Ltd., Beijing, China). A Nicolet iS50 Fourier transform infrared (FTIR) spectrometer (Thermo Scientific, Warszawa, Poland) was used to record infrared spectra using the KBr pellet method over the range of  $400\text{--}4000\text{ cm}^{-1}$  in a transmission mode. For the postmortem XPS and SEM analyses and ex situ XRD measurements, the electrode samples were retrieved from the cells at different conditions (cycled or charged/discharged to different voltages), washed with dimethyl carbonate (DMC), and vacuum dried at  $80\text{ }^\circ\text{C}$ .

### 2.3. Electrochemical Testing

The cathode slurry, made with 80 wt.% active material, 10 wt.% PVDF (Kynar 761), and 10 wt.% Super P (MTI Corp, Shenzhen, China) was cast onto carbon-coated aluminum foils (thickness:  $18\text{ }\mu\text{m}$ , MTI Corp, Shenzhen, China) before overnight vacuum drying at  $120\text{ }^\circ\text{C}$ . After drying, the electrodes were punched into circular electrode sheets with a diameter of 12 mm. The mass loading of the active material was approximately  $2\text{ mg cm}^{-2}$ . CR2032 coin cells were assembled in an argon-filled glove box ( $\text{H}_2\text{O}/\text{O}_2 < 1\text{ ppm}$ ) using 1.0 M  $\text{NaClO}_4$  in ethylene carbonate (EC):propylene carbonate (PC) = 1:1 vol% with 5.0% fluoroethylene carbonate (FEC) (NC-004, Suzhou Duoduo Chemical Technology Co., Ltd., Suzhou, China) as the electrolyte and glass-fiber filter paper (GF/F, Whatman, England) as the separator. Galvanostatic cycling of all cells was conducted on a NEWARE-BTS battery tester. Cyclic voltammetry (CV) was conducted on a Chenhua CHI760e electrochemical workstation at a scan rate of  $0.1\text{ mV s}^{-1}$ . Electrochemical impedance spectroscopy (EIS) analysis was conducted in the range of  $10^6\text{ Hz}$  to  $10^{-2}\text{ Hz}$  with an amplitude of 20 mV on a Gamry REF620 potentiostat/galvanostat analyzer. Galvanostatic intermittent titration technique (GITT) measurements were performed by charging/discharging the cells at 0.1 C for 10 min, followed by an open-circuit relaxation for 1 h. For the conductivity measurements, the pellet samples were evenly coated with silver paste on both sides and dried at  $80\text{ }^\circ\text{C}$  for 12 h. The electrical conductivity was analyzed by combining the AC impedance and DC polarization methods. The DC polarization test was carried out by recording the voltage

profile under a constant current of 0.1  $\mu\text{A}$ . Different from the EIS measurements for the liquid-state Na-ion half cells, here, the impedance spectra of the solid-state Ag | NNMO | Ag and Ag | NLNMOF | Ag cells were measured in a frequency range of 0.01 Hz–1 MHz with a slightly higher amplitude of 50 mV, considering their potentially larger cell resistances. All cells in this work were tested in an incubator (Neware, CT-9004, Guangdong, China) set constantly at 25  $^{\circ}\text{C}$ .

### 3. Results and Discussion

To identify the less explored effect of anion–cation dual doping, we successfully prepared the pristine and  $\text{Li}^+/\text{F}^-$ -modified NLNMOF materials and comparatively studied their structural and electrochemical properties as cathodes for SIBs. To start, Figure 1a illustrates the crystal structures before and after doping, where the  $\text{Li}^+$  ions tend to occupy the TM sites and the  $\text{F}^-$  ions occupy the O sites in the doped structure [33,36]. Figure 1b demonstrates the XRD patterns of NNMO and NLNMOF, with their main diffraction peaks well indexed to the hexagonal phase system (JCPSD No. 54-0894). The enlarged view of the (002) peaks reveals a slight shift to the right after doping, indicating a shrinkage along the  $c$ -axis, which is most likely due to the smaller ionic radius of  $\text{F}^-$  (133 pm) compared to  $\text{O}^{2-}$  (140 pm) [37]. The drop in the  $c$  parameter is also confirmed by the Rietveld refinement results shown in Figure 1c,d. The slight increase in the  $a$ -axis parameter may be related to the substitution of  $\text{Ni}^{2+}$  (69 pm) and  $\text{Mn}^{4+}$  (53 pm) with  $\text{Li}^+$  (76 pm) with a larger radius. The SEM images for both samples are displayed in Figure 1e,f. NNMO exhibits surface-smooth primary particles in a plate shape and with sharp edges, while the NLNMOF particles show roughened surfaces with more round edges, which is similar to the observation seen for the F-doped NNMO samples reported by Chen et al. [33]. The EDS mapping, shown in Figure 1g–l, indicates that all elements, including F, are uniformly distributed.

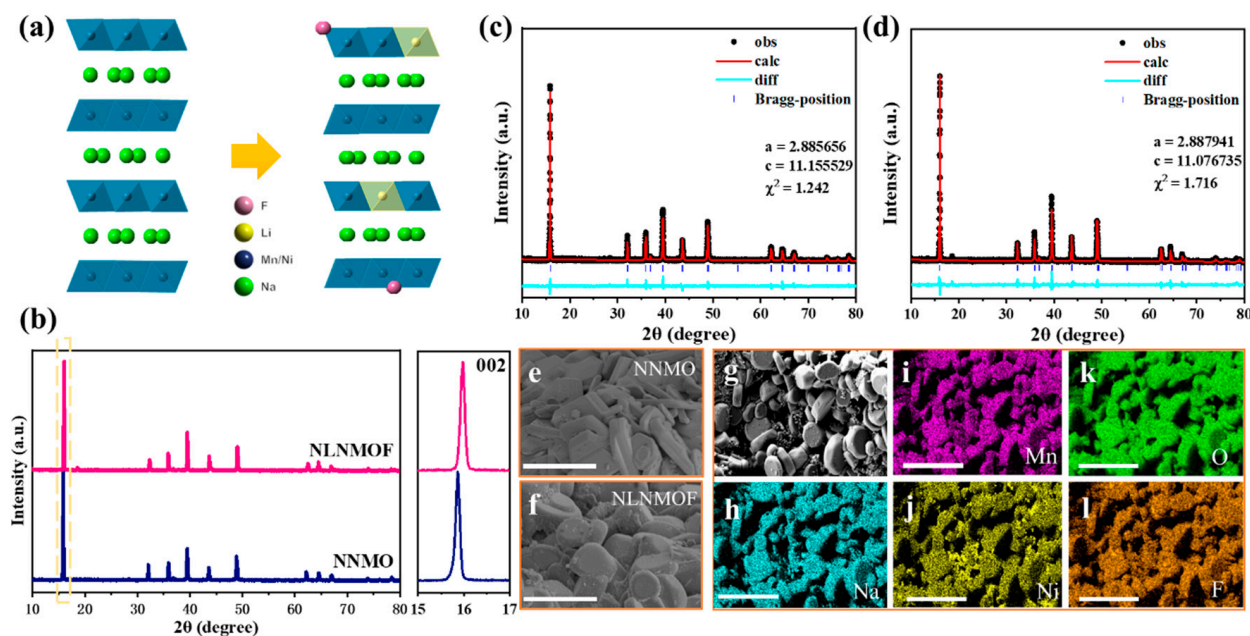


**Figure 1.** (a) Schematic illustration of the crystal structures of NNMO and NLNMOF. (b) XRD patterns of NNMO and NLNMOF with the (002) peaks enlarged on the right. Rietveld refinement results of (c) NNMO and (d) NLNMOF. SEM images of (e) NNMO and (f) NLNMOF, with the corresponding EDX maps for NLNMOF displayed in (g–l). Scale bars: 5  $\mu\text{m}$  in (e,f) and 10  $\mu\text{m}$  in (g–l).

XPS was used to characterize the elemental compositions. First, the Mn element maintained +4 valence before and after doping (Figure 2a,b), with the peaks at 642.1 eV and 653.6 eV corresponding, respectively, to the Mn  $2p_{3/2}$  and  $2p_{1/2}$  [13]. The  $\text{Mn}^{4+}$  ions

are widely believed to inhibit the cooperative Jahn–Teller effect and stabilize the layered structure [38]. As shown in Figure 2c,d, The Ni 2p spectra exhibit two sets of doublets from Ni<sup>2+</sup> (854.2 eV and 871.7) and Ni<sup>3+</sup> (855.6 eV and 873.0 eV), [13] and their estimated proportions are listed in Table S2. The percentage of Ni<sup>2+</sup> is 63.7% for NNMO, which climbs to 74.7% after Li/F doping [21]. The successful incorporation of Li into NLNMOF is further confirmed by the XPS Li 1s spectrum shown in Figure S1. As can be seen in Figure 2e, F exists in two forms, with one forming TM–F bonds in NLNMOF, as characterized by the peak at 686.7 eV, while the other points to Na–F bonds in NaF, as characterized by the peak at 685 eV [39,40]. This indicates F not only enters the lattice of NLNMOF but forms NaF on the surface. The FTIR spectra (Figure 2f) were acquired to identify more surface characteristics. Notably, after Li/F doping, the vibration peaks at 642, 1407, and 3446 cm<sup>−1</sup> related to the O–H stretch (i.e., from OH<sup>−</sup>/HCO<sub>3</sub><sup>−</sup>) being significantly weakened, suggesting improved moisture stability. This is likely due to the formation of stronger TM–F bonds in the lattice and chemically stable NaF on the surface (Figure 2e) [41,42]. The O 1s spectra were also analyzed (Figure S2), where surface oxygen species characterized by peaks at 529.1 and 532.6 eV reduced after doping, suggesting the better surface stability of NLNMOF [43]. The Raman spectra of both samples reveal two major bands at 589 cm<sup>−1</sup> (A<sub>1g</sub>, unsymmetric stretching vibration of TM–O bonds, TM: Ni, Mn) and 482 cm<sup>−1</sup> (bending vibration of O–TM–O bonds), as shown in Figure S3 [44]. The slight red shift of the E<sub>g</sub> peak, induced by Li/F doping, can be ascribed to the enlarged unit cell parameter *a*, as evidenced by XRD analysis (Figure 1c,d), while the drop in the ratio of I<sub>Eg</sub>/I<sub>A1g</sub> indicates the compression of the transitional metal layer and the expansion of the planar oxygen layer after Li/F incorporation, which tends to benefit Na<sup>+</sup> extraction [45].

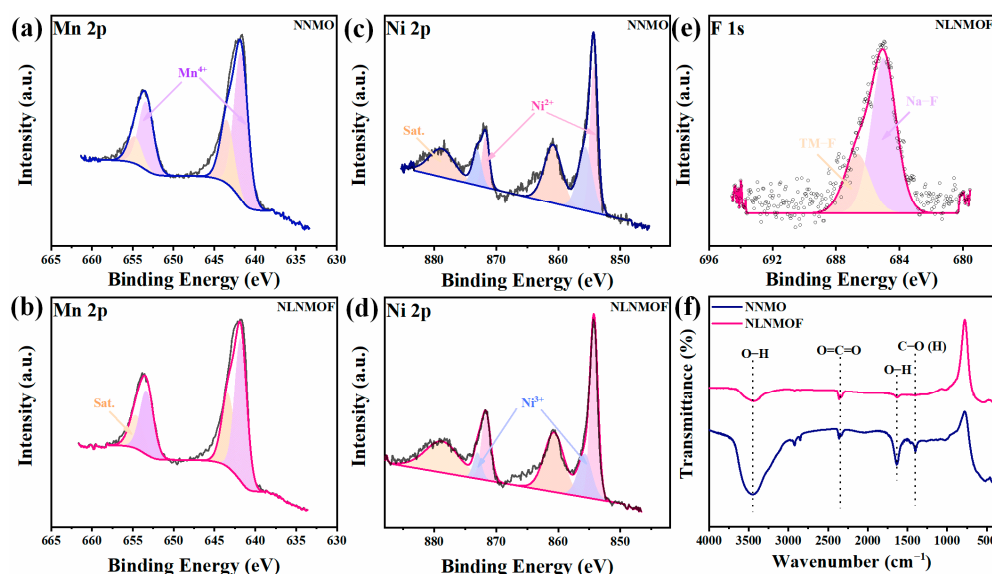


**Figure 2.** XPS spectra of NNMO and NLNMOF, (a,b) Mn 2p, (c,d) Ni 2p, and (e) F 1s. (f) FTIR spectra of NNMO and NLNMOF.

The electrochemical performance of both electrodes was evaluated in coin cells with Na metal as the anode. Except at the initial five cycles at 0.1 C, the NLNMOF electrode delivered consistently higher capacities at all tested rates (Figure 3a). Even at a high C-rate of 10 C, the NLNMOF electrode outputted a capacity of 63.4 mAh g<sup>−1</sup>, significantly outperforming that of NNMO (15.8 mAh g<sup>−1</sup>). The cyclability of NNMO and NLNMOF is compared in Figure 3b. After five activation cycles at 0.1 C, the cells were cycled at 0.5 C between 2.0–4.3 V. The NNMO electrode had an initial capacity of 133.8 mAh g<sup>−1</sup>, which dropped dramatically during the activation process, ending at only 47.6 mAh g<sup>−1</sup> after 100 cycles. The NLNMOF electrode, despite its slightly lower initial capacity of 127.1 mAh g<sup>−1</sup>, retained 81.9 mAh g<sup>−1</sup> after 100 cycles. The voltage profiles of both electrodes during

long-term cycling were compared. As shown in Figure 3c, the capacity of the NNMO cell decreased rapidly within the first 10 cycles. This capacity fading has been widely ascribed to the P2–O2 phase transition and Na<sup>+</sup>/vacancy ordering [46,47]. Particularly, the P2–O2 phase transition above 4.0 V can cause lattice mismatch and dislocation, leading to the destruction of active particles and fast capacity decay [48]. At first glance, the charge/discharge curves of NLNMOF are relatively smooth without obvious plateaus (Figure 3d), indicating that the Na intercalation/deintercalation proceeded via a solid solution mechanism [21,49]. It has been experimentally proven that Li<sup>+</sup> ions preferentially reside in the transition-metal layer, stabilizing the P2 structure in the voltage range of 2.0–4.3 V by migrating to Na layers at high voltages and shuttling back to transition-metal layers at low voltages [19]. More structure insights will be provided in detail with the help of the in situ Raman and ex situ XRD analyses.

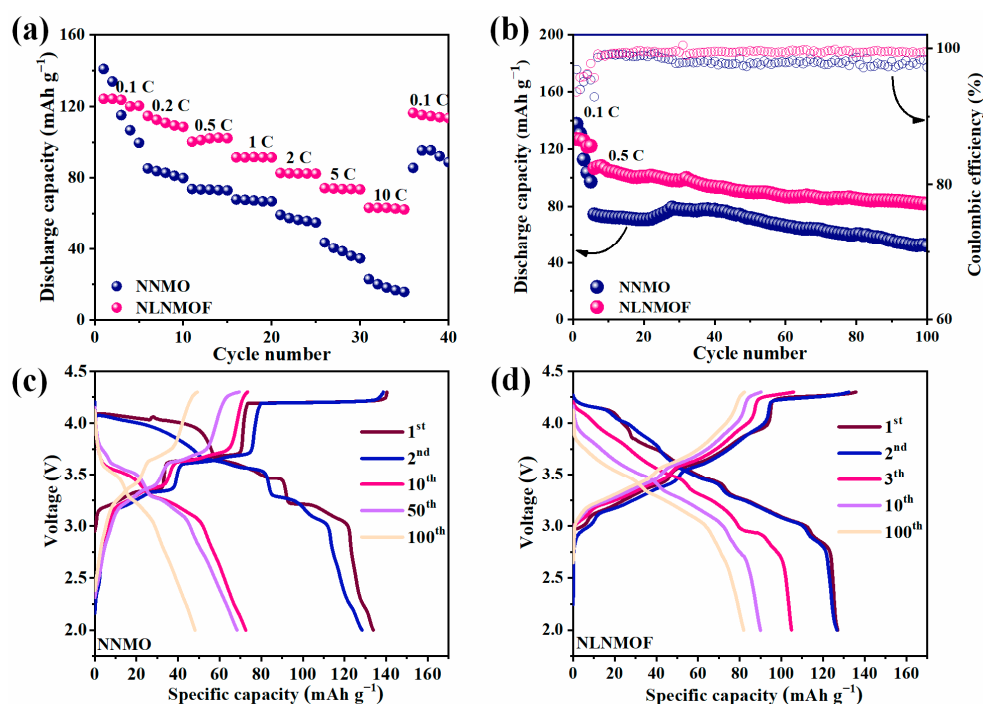


**Figure 3.** (a) Rate and (b) cycling performances of NNMO and NLNMOF electrodes between 2.0–4.3 V. The charge–discharge profiles of (c) NNMO and (d) NLNMOF for the 1<sup>st</sup>, 2<sup>nd</sup>, 10<sup>th</sup>, 50<sup>th</sup>, and 100<sup>th</sup> cycle.

To identify the role of the single F modification on cyclability, Figure S4 compares the cycling performance of NNMO and F-doped NNMO. The better capacity retention of NNMOF may be related to the stronger TM–F bonds (relative to TM–O bonds), as calculated by Mao et al. [50], which can mitigate the structural changes during cycling by inhibiting the slide of TMO<sub>2</sub> layers. In addition, we believe that NaF formed on the surface can also, to some extent, mitigate the electrolyte attack during cycling. The identical plateaus of the NNMO and F-modified NNMO electrodes indicate a similar electrochemical reaction mechanism (Figure S4b) [32,34]. The increase in capacity utilization is due to the enhancement of the electrical conductivity of NNMO, which will be further discussed in the next section. Obviously, the F-modified electrode still showed a rapid capacity drop in the first few cycles (Figure S4a). Therefore, the improvement in structural stability and, thus, cyclability witnessed for NLNMOF is predominantly induced by Li incorporation. We also examined both electrodes at 4.5 V (Figure S5), and the results verify that the Li<sup>+</sup>/F<sup>-</sup> modification can consistently promote both the rate and cycling performance of NNMO.

In order to probe the structural evolution of NNMO and NLNMOF electrodes during the charging and discharging process, the ex situ XRD patterns were collected (Figure 4).

The (002) peaks are enlarged on the left to illustrate the major trend. For NNMO, the (002) peak shifts to a lower angle with charging, indicating the expansion along the *c*-axis and the increase of the layer spacing; [16] during discharging, it shifts back to its original position. However, the (002) peak disappears above 4.0 V, while an extra peak, located at 20°, appears, disclosing the presence of a harmful P2–O2 phase transition (Figure 4a) [51]. The evolution of the (002) peak for NLNMOF follows a similar route, except there is no O2 phase formation (Figure 4b). Monitoring the (004) peaks of NNMO and NLNMOF returns the same trend. Obviously, the P2-layered structure of NLNMOF can be well maintained during the charging/discharging process, as the extraction and insertion of Na<sup>+</sup> in NLNMOF proceeds via a highly reversible P2–P2 solid solution reaction [52]. It should be noted here that the peaks at 12.5° and 25.2° are hydrated phases, most likely introduced during the sample preparation process. It has been frequently reported that when the Na<sup>+</sup> content is less than 1/3, there is a strong tendency for NNMO to absorb water and form hydrated phases [51,53]. Postmortem electrode characterizations were conducted to support the ex situ XRD analysis. Figure S6 shows the XRD patterns of both cathodes after cycling, where NLNMOF still exhibits a well-defined P2-type structure. In stark contrast, some peaks belonging to the P2 structure significantly weaken and even disappear for the cycled NNMO. This provides evidence for the irreversible P2–O2 phase transition that has led to the decrease of crystallinity and serious destruction of the crystal structure [54,55].

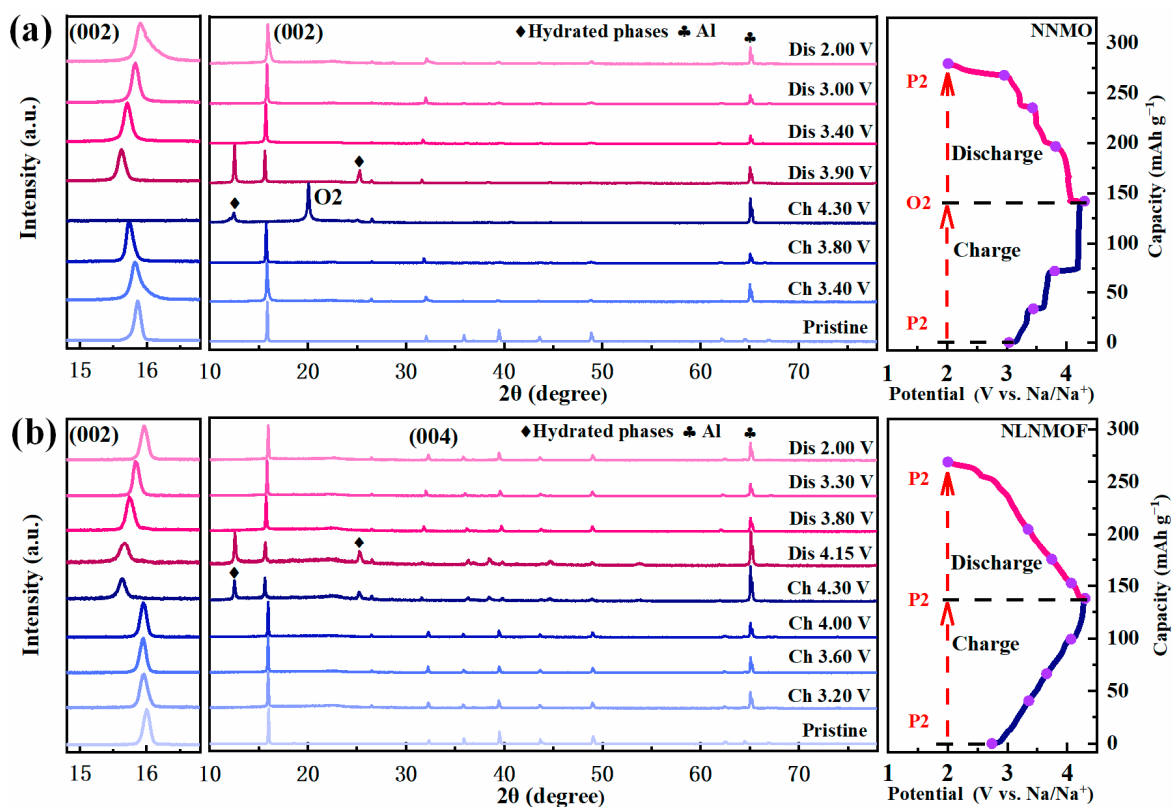


**Figure 4.** Ex situ XRD patterns acquired on electrodes retrieved from cells stopped at different stages during the first cycle of (a) NNMO and (b) NLNMOF electrodes.

A more sensitive in situ Raman analysis was employed to capture the microscopic structure changes. The spectra of both NNMO and NLNMOF are displayed in Figure 5, with assignments of the major Raman peak positions summarized in Table S3. Initially, NNMO has two distinct Raman peaks, located at approximately 476 cm<sup>-1</sup> and 584 cm<sup>-1</sup>, corresponding to the *E<sub>g</sub>* and *A<sub>1g</sub>* modes, respectively, for the TM–O arrangements in the layered structure. With charging the cell, the *E<sub>g</sub>* peak gradually weakens and finally vanishes at 3.63 V, accompanied by the appearance of a 513 cm<sup>-1</sup> peak for the vibration

mode of  $\text{Ni}^{3+}$  [56]. Meanwhile, the  $584\text{ cm}^{-1}$  ( $A_{1g}$  peak) gradually shifts to  $574\text{ cm}^{-1}$ . When charging the cell to 4.22 V, the  $E_g$  peak completely disappears, as most  $\text{Na}^+$  ions are extracted [13]. At this stage, the  $574\text{ cm}^{-1}$  peak corresponding to the vibration mode of  $\text{Mn}^{4+}$  strengthens, and the peak position is very close to that reported for  $\delta\text{-MnO}_2$  [57]. Concomitantly, the  $\text{Ni}^{3+}$  peak at  $513\text{ cm}^{-1}$  slightly shifts to  $517\text{ cm}^{-1}$ , reported for the O–Ni–O stretching vibration in  $\text{NiO}_6$  [58]. Clearly,  $\text{O}_2\text{-Ni}_{1/3}\text{Mn}_{2/3}\text{O}_2$  has become the main configuration above 4.22 V. During discharging, most of the peaks return to their initial positions. However, it is worth noting that, after a single cycle, the  $A_{1g}$  peak reveals a red shift relative to its initial value ( $584$  vs.  $580\text{ cm}^{-1}$ ), implying that an irreversible structural change has occurred. The major trend of NLNMOF is similar to that of NNMO, with two important differences emphasized below. First, the intrinsic  $E_g$  vibration peak of NLNMOF is better preserved, and all peaks return to their original positions [13]. Moreover, it is observed that the bonding environment of  $\text{Mn}^{4+}$  differs from that of NNMO at a high state of charge. With charging the cell to above around 3.62 V, the peak at  $659\text{ cm}^{-1}$  for the vibration mode of  $\text{Mn}^{4+}$  appears instead of that at  $574\text{ cm}^{-1}$  for NNMO. We noticed that this peak at  $659\text{ cm}^{-1}$  matches better with that of  $\beta\text{-MnO}_2$  or  $\lambda\text{-MnO}_2$  rather than  $\delta\text{-MnO}_2$  [57]. This difference arises, most likely as a result of the distinct bonding environments for  $\text{Mn}^{4+}$  in the P2 and O2 structures. Overall, the capability of NLNMOF to circumvent the P2–O2 phase transition and maintain its structural integrity during high-voltage cycling is further verified by the in situ Raman analysis.

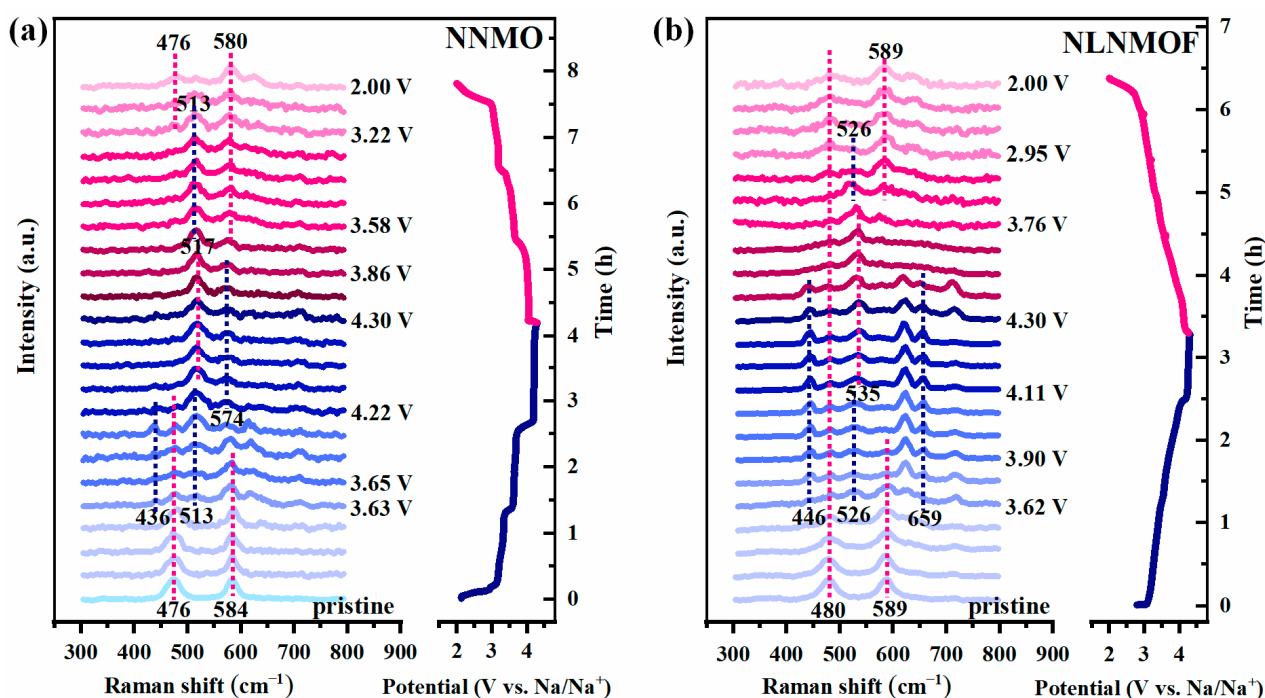


**Figure 5.** In situ Raman spectra of (a) NNMO and (b) NLNMOF electrodes acquired during the first cycle.

After resolving the enhancement mechanisms, in terms of structural stability, we next turn to understand the reasons behind the superior rate capability of NLNMOF. For the kinetic analysis of electrode materials, the solid-state ion diffusion within electrode materials is usually deemed the rate-determine step, and electroanalytic techniques, such as GITT, EIS, and CV, are commonly used to determine the ion diffusivity. However, these techniques are applied in a coin cell containing the electrode made from the active material, the counter electrode (i.e., Li, Na metal), and the liquid electrolyte. In such a complex configuration, the acquired data are affected by multiple transport processes occurring in not only the electrode material but also the liquid electrolyte inside the

porous electrode [59]. Herein, we applied Ag paste on both sides of a sintered NNMO or NLNMO pellet to construct ion-blocking electrodes (inset, Figure 6a) and performed conductivity measurements based on EIS and DC polarization in order to directly measure the electrical conductivities of the bulk cathode materials. As shown in Figure 6a, the EIS spectra of both pellets reveal a high-frequency semicircle and a low-frequency slope, typical characteristics of an ionic-conductivity-dominated behavior normally observed for solid electrolytes [60,61]. The equivalent circuit used for fitting is also displayed in the inset of Figure 6a. Notably, the fitted total resistance ( $R_{total}$ ) of NNMO is way larger than that of NLNMOF. The ionic conductivities ( $\sigma_{Na^+}$ ) of the NNMO and NLNMOF pellets were estimated, based on the fitted resistances and sample dimensions, to be  $1.8 \times 10^{-7} \text{ S cm}^{-1}$  and  $8.5 \times 10^{-6} \text{ S cm}^{-1}$ , respectively. The DC polarization curves were also acquired by monitoring the voltage response under a small and constant current, as shown in Figure S7 [62]. According to the equilibrium voltage, the electronic conductivity of NLNMOF was calculated to be  $2.4 \times 10^{-8} \text{ S cm}^{-1}$ , which is also slightly higher than that of NNMO ( $1.1 \times 10^{-8} \text{ S cm}^{-1}$ ). This result, especially the nearly two-magnitude improvement in ionic conductivity by Li/F modification, offers direct evidence for the superior rate performance of NLNMOF.

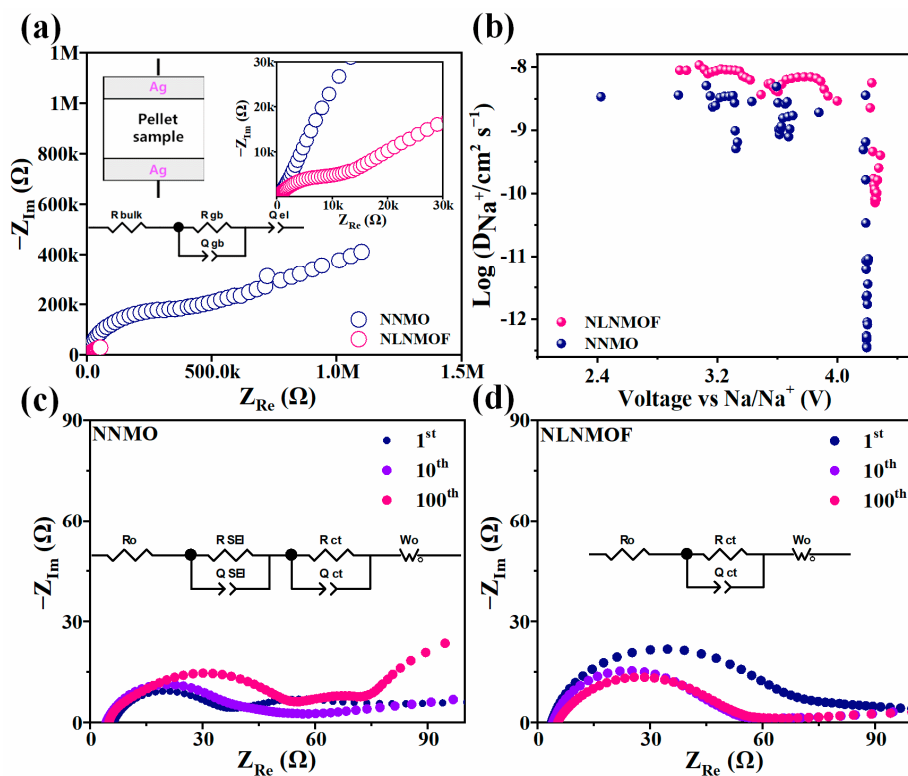


**Figure 6.** (a) Nyquist plots for NNMO and NLNMOF pellets coated with Ag paste on both sides and the corresponding fitting curves. (b) The sodium-ion diffusion coefficient ( $D_{Na^+}$ ) of Na/NNMO cell and Na/NLNMOF cell cycling between 2.0 V and 4.3 V for the charge states of the first cycle. Nyquist plot of (c) NNMO and (d) NLNMOF, respectively, and the equivalent circuit is shown in the inset.

In order to provide voltage-dependent kinetic information, GITT measurements were also conducted. The calculated diffusivity values were plotted in Figure 6b for both electrodes as a function of voltage vs. Na/Na<sup>+</sup>, with the testing data and an example of the calculation provided in Figure S8. The sodium-ion diffusivity ( $D_{Na^+}$ ) values of NLNMOF are significantly higher than those of NNMO throughout the testing potentials. Particularly, the  $D_{Na^+}$  of NNMO shows a drastic drop when above 4.0 V, where a widening gap between NNMO and NLNMOF is evident. This may be due to the fact that Na<sup>+</sup> must migrate through the tetrahedral gap between two octahedra in the O2 structure,

which is more energetically difficult than that in the special triangular prism structure of P2, where  $\text{Na}^+$  can be directly transported through the adjacent shared faces [63]. In summary, both conductivity and GITT measurements point to the faster  $\text{Na}^+$  diffusion in NLNMOF. Furthermore, EIS spectra before cycling and after 10 and 100 cycles were measured, as shown in Figure 6c,d, with the specific fitting results listed in Table S4, where  $R_0$  is the ohmic resistance from the solution resistance and the wire connection;  $R_{\text{SEI}}$  is the resistance of the solid electrolyte interphase (SEI);  $R_{\text{ct}}$  is the charge-transfer resistance at the electrode–electrolyte interface; and  $W_0$  represents the Warburg diffusion process. When  $R_{\text{SEI}}$  cannot be well separated from  $R_{\text{ct}}$ , one semicircle was fitted to determine the  $R_{\text{ct}}$ , as is the case for all spectra of NLNMOF. Apparently, NLNMOF showed smaller and more stable  $R_{\text{ct}}$  throughout the cycling process. After 100 cycles, the total resistances of NLNMOF and NNMO are, respectively, 47.5 ohm and 86.2 ohm, with the biggest difference being contributed by  $R_{\text{ct}}$ . The EIS analysis proves a more favorable charge-transfer process in the NLNMOF cell, which is consistent with its superior electrochemical performance (Figure 3).

In order to showcase the broad application of the P2-NLNMOF cathode, the solid-state cells were successfully assembled and evaluated (Figure 7). The schematic of the solid-state battery is shown in Figure 7c. A NASICON-type  $\text{Na}_3\text{Zr}_2\text{Si}_2\text{PO}_{12}$  (NZSP) was used as the solid electrolyte, and a Pb/C wetting agent was employed to improve the NZSP | Na interface contact and enable the controllable Na anode loading. More details for the synthesis and interface modification are referred to in our previous work [64]. Benefiting from the perfect Na wetting, enabled by the Pb/C coated NZSP (Pb/C@NZSP) and the fast cathode reaction kinetics in NLNMOF, the solid-state sodium-metal battery delivered a high initial capacity of  $146.07 \text{ mAh g}^{-1}$  at 0.1 C and could retain  $101.68 \text{ mAh g}^{-1}$  at 1 C (Figure 7a). The voltage profiles for the first two cycles during the long-term cycling at 0.5 C are displayed in Figure 7b, demonstrating an initial capacity of near  $120 \text{ mAh g}^{-1}$  and very identical and smooth charging/discharging curves. After 100 cycles, the cell showed a high-capacity retention rate of 72.3% (Figure 7c). The inset of Figure 7c demonstrates that the LED screen can be lit by a single solid-state sodium-metal battery (SSSMB).

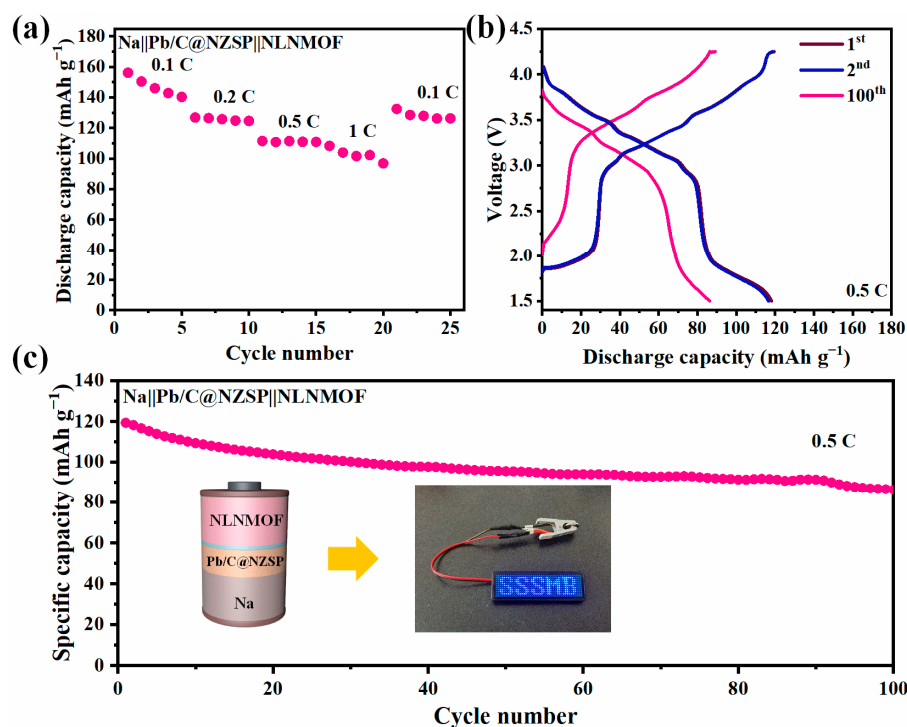


**Figure 7.** (a) The rate and (c) cycling performance of the solid-state Na || Pb/C@NZSP || NLNMOF battery between 1.5 V and 4.25 V. (b) The charge–discharge profiles for the 1st, 2nd, and 100th cycles.

#### 4. Conclusions

In summary, we propose a  $\text{Li}^+/\text{F}^-$  modification strategy to improve the electrochemical performance of P2-type NNMO cathode materials. The modified NLNMOF materials showed improved surface stability against moisture, benefiting from the formation of strong transition-metal–F bonds and a NaF surface layer. More importantly, the resulting electrode delivered a significantly higher capacity retention rate (64% vs. 36%, 100 cycles) at 0.5 C and a four-times higher capacity output at 10 C, relative to the pristine one. The cyclability enhancement mechanisms were explored by combining the ex situ XRD and in situ Raman analysis. It was discovered that NLNMOF follows a highly reversible P2–P2 solid-solution reaction when cycled between 2.0–4.3 V, circumventing the harmful P2–O2 phase transition and  $\text{Na}^+$ /vacancy ordering that has led to the structural deterioration of NNMO. Via the conductivity measurements and GITT analysis, we verified on both the bulk material and electrode levels,  $\text{Li}^+/\text{F}^-$  substitution can greatly accelerate solid-state  $\text{Na}^+$  conduction, thereby achieving a notable rate improvement. The superior performance of NLNMOF cathodes was also demonstrated in an SSSMB to broaden its application. The present cation/anion modification strategy is expected to open new opportunities towards the rational design of high-performance layered cathode materials for SIBs.

**Supplementary Materials:** The following supporting information can be downloaded at: <https://www.mdpi.com/article/10.3390/coatings13030626/s1>, Figures S1–S3: XPS and Raman data; Figures S4 and S5: cycling data; Figure S6: XRD; Figure S7: DC polarization curve; Figure S8: GITT data; Table S1: synthesis recipes; Table S2: XPS analysis results; Table S3: Raman analysis results; Table S4: EIS analysis results [65].

**Author Contributions:** X.C. conducted the experiments; W.G., R.L. and P.D. helped carry out the cell test experiments; X.C. and X.Z. collectively wrote the paper; X.Z. and S.G. supervised the project. All authors have read and agreed to the published version of the manuscript.

**Funding:** The authors are grateful for financial support from the National Natural Science Foundation of China (52202199), the Anhui Provincial Natural Science Foundation (2108085QE202), and start-up grants from Anhui University (S020318008/007, S020118002/060).

**Institutional Review Board Statement:** Not applicable.

**Informed Consent Statement:** Not applicable.

**Data Availability Statement:** Data is contained within the article.

**Conflicts of Interest:** The authors declare no competing financial interest.

#### References

1. Winter, M.; Barnett, B.; Xu, K. Before Li Ion Batteries. *Chem. Rev.* **2018**, *118*, 11433–11456. [CrossRef]
2. Li, M.; Lu, J.; Chen, Z.; Amine, K. 30 Years of Lithium-Ion Batteries. *Adv. Mater.* **2018**, *118*, 1800561. [CrossRef] [PubMed]
3. Hwang, J.Y.; Myung, S.T.; Sun, Y.K. Sodium-ion batteries: Present and future. *Chem. Soc. Rev.* **2017**, *46*, 3529–3614. [CrossRef]
4. Chayambuka, K.; Mulder, G.; Danilov, D.L.; Notten, P.H.L. Sodium-Ion Battery Materials and Electrochemical Properties Reviewed. *Adv. Energy Mater.* **2018**, *8*, 1800079. [CrossRef]
5. Usiskin, R.; Lu, Y.; Popovic, J.; Law, M.; Balaya, P.; Hu, Y.-S.; Maier, J. Fundamentals, status and promise of sodium-based batteries. *Nat. Rev. Mater.* **2021**, *6*, 1020–1035. [CrossRef]
6. Xu, Z.; Wang, J. Toward Emerging Sodium-Based Energy Storage Technologies: From Performance to Sustainability. *Adv. Energy Mater.* **2022**, *12*, 2201692. [CrossRef]
7. Su, H.; Jaffer, S.; Yu, H. Transition metal oxides for sodium-ion batteries. *Energy Storage Mater.* **2016**, *5*, 116–131. [CrossRef]
8. Xiao, J.; Li, X.; Tang, K.; Wang, D.; Long, M.; Gao, H.; Chen, W.; Liu, C.; Liu, H.; Wang, G. Recent progress of emerging cathode materials for sodium ion batteries. *Mater. Chem. Front.* **2021**, *5*, 3735–3764. [CrossRef]
9. Liu, Q.; Hu, Z.; Chen, M.; Zou, C.; Jin, H.; Wang, S.; Chou, S.L.; Dou, S.X. Recent Progress of Layered Transition Metal Oxide Cathodes for Sodium-Ion Batteries. *Small* **2019**, *15*, 1805381. [CrossRef] [PubMed]
10. Wang, S.; Sun, C.; Wang, N.; Zhang, Q. Ni- and/or Mn-based layered transition metal oxides as cathode materials for sodium ion batteries: Status, challenges and countermeasures. *J. Mater. Chem. A* **2019**, *7*, 10138–10158. [CrossRef]
11. Xiao, Y.; Abbasi, N.M.; Zhu, Y.F.; Li, S.; Tan, S.J.; Ling, W.; Peng, L.; Yang, T.; Wang, L.; Guo, X.D.; et al. Layered Oxide Cathodes Promoted by Structure Modulation Technology for Sodium-Ion Batteries. *Adv. Funct. Mater.* **2020**, *30*, 2001334. [CrossRef]

12. Gabriel, E.; Hou, D.; Lee, E.; Xiong, H. Multiphase layered transition metal oxide positive electrodes for sodium ion batteries. *Energy Sci. Eng.* **2022**, *10*, 1672–1705. [[CrossRef](#)]
13. Peng, B.; Sun, Z.; Zhao, L.; Li, J.; Zhang, G. Dual-Manipulation on P2-Na<sub>0.67</sub>Ni<sub>0.33</sub>Mn<sub>0.67</sub>O<sub>2</sub> Layered Cathode toward Sodium-Ion Full Cell with Record Operating Voltage Beyond 3.5 V. *Energy Storage Mater.* **2021**, *35*, 620–629. [[CrossRef](#)]
14. Li, W.; Yao, Z.; Zhang, S.; Wang, X.; Xia, X.; Gu, C.; Tu, J. Exploring the Stability Effect of the Co-Substituted P2-Na<sub>0.67</sub>[Mn<sub>0.67</sub>Ni<sub>0.33</sub>]O<sub>2</sub> Cathode for Liquid- and Solid-State Sodium-Ion Batteries. *ACS Appl. Mater. Interfaces* **2020**, *12*, 41477–41484. [[CrossRef](#)] [[PubMed](#)]
15. Chu, S.; Guo, S.; Zhou, H. Advanced cobalt-free cathode materials for sodium-ion batteries. *Chem. Soc. Rev.* **2021**, *50*, 13189–13235. [[CrossRef](#)]
16. Lu, Z.; Dahn, J.R. In Situ X-Ray Diffraction Study of P2-Na<sub>2/3</sub>Ni<sub>1/3</sub>Mn<sub>2/3</sub>O<sub>2</sub>. *J. Electrochem. Soc.* **2001**, *148*, A1225. [[CrossRef](#)]
17. Liu, Q.; Hu, Z.; Chen, M.; Zou, C.; Jin, H.; Wang, S.; Gu, Q.; Chou, S. P2-type Na<sub>2/3</sub>Ni<sub>1/3</sub>Mn<sub>2/3</sub>O<sub>2</sub> as a cathode material with high-rate and long-life for sodium ion storage. *J. Mater. Chem. A* **2019**, *7*, 9215–9221. [[CrossRef](#)]
18. Lee, D.H.; Xu, J.; Meng, Y.S. An advanced cathode for Na-ion batteries with high rate and excellent structural stability. *Phys. Chem. Chem. Phys.* **2013**, *15*, 3304–3312. [[CrossRef](#)]
19. Clément, R.J.; Xu, J.; Middlemiss, D.S.; Alvarado, J.; Ma, C.; Meng, Y.S.; Grey, C.P. Direct evidence for high Na<sup>+</sup> mobility and high voltage structural processes in P2-Na<sub>x</sub>[Li<sub>y</sub>Ni<sub>z</sub>Mn<sub>1-y-z</sub>]O<sub>2</sub> ( $x, y, z \leq 1$ ) cathodes from solid-state NMR and DFT calculations. *J. Mater. Chem. A* **2017**, *5*, 4129–4143. [[CrossRef](#)]
20. Bai, X.; Sathiya, M.; Mendoza-Sánchez, B.; Iadecola, A.; Vergnet, J.; Dedryvère, R.; Saubanère, M.; Abakumov, A.M.; Rozier, P.; Tarascon, J.-M. Anionic Redox Activity in a Newly Zn-Doped Sodium Layered Oxide P2-Na<sub>2/3</sub>Mn<sub>1-y</sub>Zn<sub>y</sub>O<sub>2</sub> ( $0 < y < 0.23$ ). *Adv. Energy Mater.* **2018**, *8*, 1802379.
21. Chen, Y.; Su, G.; Cheng, X.; Du, T.; Han, Y.; Qiang, W.; Huang, B. Electrochemical performances of P2-Na<sub>2/3</sub>Ni<sub>1/3</sub>Mn<sub>2/3</sub>O<sub>2</sub> doped with Li and Mg for high cycle stability. *J. Alloys Compd.* **2021**, *858*, 157717. [[CrossRef](#)]
22. Shi, Q.; Qi, R.; Feng, X.; Wang, J.; Li, Y.; Yao, Z.; Wang, X.; Li, Q.; Lu, X.; Zhang, J.; et al. Niobium-doped layered cathode material for high-power and low-temperature sodium-ion batteries. *Nat. Commun.* **2022**, *13*, 3205. [[CrossRef](#)] [[PubMed](#)]
23. Zhang, Y.; Wu, M.; Ma, J.; Wei, G.; Ling, Y.; Zhang, R.; Huang, Y. Revisiting the Na<sub>2/3</sub>Ni<sub>1/3</sub>Mn<sub>2/3</sub>O<sub>2</sub> Cathode: Oxygen Redox Chemistry and Oxygen Release Suppression. *ACS Cent. Sci.* **2020**, *6*, 232–240. [[CrossRef](#)]
24. Dang, R.; Chen, M.; Li, Q.; Wu, K.; Lee, Y.L.; Hu, Z.; Xiao, X. Na<sup>+</sup>-Conductive Na<sub>2</sub>Ti<sub>3</sub>O<sub>7</sub>-Modified P2-type Na<sub>2/3</sub>Ni<sub>1/3</sub>Mn<sub>2/3</sub>O<sub>2</sub> via a Smart in Situ Coating Approach: Suppressing Na<sup>+</sup>/Vacancy Ordering and P2-O<sub>2</sub> Phase Transition. *ACS Appl. Mater. Interfaces* **2019**, *11*, 856–864. [[CrossRef](#)] [[PubMed](#)]
25. Ji, H.; Zhai, J.; Chen, G.; Qiu, X.; Fang, H.; Zhang, T.; Huang, Z.; Zhao, W.; Wang, Z.; Chu, M.; et al. Surface Engineering Suppresses the Failure of Biphasic Sodium Layered Cathode for High Performance Sodium-Ion Batteries. *Adv. Funct. Mater.* **2021**, *32*, 2109319. [[CrossRef](#)]
26. Li, H.; Wang, T.; Wang, X.; Li, G.; Du, Y.; Shen, J.; Chai, J. Sodium superionic conductor NaTi<sub>2</sub>(PO<sub>4</sub>)<sub>3</sub> surface layer modified P2-type Na<sub>2/3</sub>Ni<sub>1/3</sub>Mn<sub>2/3</sub>O<sub>2</sub> as high-performance cathode for sodium-ion batteries. *J. Power Sources* **2021**, *494*, 229771. [[CrossRef](#)]
27. Liu, Y.; Fang, X.; Zhang, A.; Shen, C.; Liu, Q.; Enaya, H.A.; Zhou, C. Layered P2-Na<sub>2/3</sub>[Ni<sub>1/3</sub>Mn<sub>2/3</sub>]O<sub>2</sub> as high-voltage cathode for sodium-ion batteries: The capacity decay mechanism and Al<sub>2</sub>O<sub>3</sub> surface modification. *Nano Energy* **2016**, *27*, 27–34. [[CrossRef](#)]
28. Liu, Y.; Shen, Q.; Zhao, X.; Zhang, J.; Liu, X.; Wang, T.; Zhang, N.; Jiao, L.; Chen, J.; Fan, L.Z. Hierarchical Engineering of Porous P2-Na<sub>2/3</sub>Ni<sub>1/3</sub>Mn<sub>2/3</sub>O<sub>2</sub> Nanofibers Assembled by Nanoparticles Enables Superior Sodium-Ion Storage Cathodes. *Adv. Funct. Mater.* **2019**, *30*, 1907837. [[CrossRef](#)]
29. Wang, P.-F.; Yao, H.-R.; Liu, X.-Y.; Yin, Y.-X.; Zhang, J.-N.; Wen, Y.; Yu, X.; Gu, L.; Guo, Y.-G. Na<sup>+</sup>/vacancy disordering promises high-rate Na-ion batteries. *Sci. Adv.* **2018**, *4*, eaar6018. [[CrossRef](#)]
30. Xiao, B.; Liu, X.; Chen, X.; Lee, G.H.; Song, M.; Yang, X.; Omenya, F.; Reed, D.M.; Sprenkle, V.; Ren, Y.; et al. Uncommon Behavior of Li Doping Suppresses Oxygen Redox in P2-Type Manganese-Rich Sodium Cathodes. *Adv. Mater.* **2021**, *33*, 2107141. [[CrossRef](#)]
31. Zhang, J.; Wang, W.; Wang, W.; Wang, S.; Li, B. Comprehensive Review of P2-Type Na<sub>2/3</sub>Ni<sub>1/3</sub>Mn<sub>2/3</sub>O<sub>2</sub>, a Potential Cathode for Practical Application of Na-Ion Batteries. *ACS Appl. Mater. Interfaces* **2019**, *11*, 22051–22066. [[CrossRef](#)] [[PubMed](#)]
32. Liu, K.; Tan, S.; Moon, J.; Jafta, C.J.; Li, C.; Kobayashi, T.; Lyu, H.; Bridges, C.A.; Men, S.; Guo, W.; et al. Insights into the Enhanced Cycle and Rate Performances of the F<sup>-</sup> Substituted P2-Type Oxide Cathodes for Sodium-Ion Batteries. *Adv. Energy Mater.* **2020**, *10*, 2000135. [[CrossRef](#)]
33. Chen, H.; Wu, Z.; Zhong, Y.; Chen, T.; Liu, X.; Qu, J.; Xiang, W.; Li, J.; Chen, X.; Guo, X.; et al. Boosting the reactivity of Ni<sup>2+</sup>/Ni<sup>3+</sup> redox couple via fluorine doping of high performance Na<sub>0.6</sub>Mn<sub>0.95</sub>Ni<sub>0.05</sub>O<sub>2-x</sub>F<sub>x</sub> cathode. *Electrochim. Acta* **2019**, *308*, 64–73. [[CrossRef](#)]
34. Zhou, P.; Zhang, J.; Che, Z.; Quan, Z.; Duan, J.; Wu, X.; Weng, J.; Zhao, J.; Zhou, J. Insights into the enhanced structure stability and electrochemical performance of Ti<sup>4+</sup>/F<sup>-</sup> co-doped P2-Na<sub>0.67</sub>Ni<sub>0.33</sub>Mn<sub>0.67</sub>O<sub>2</sub> cathodes for sodium ion batteries at high voltage. *J. Energy Chem.* **2022**, *67*, 655–662. [[CrossRef](#)]
35. Cui, X.; Wang, S.; Ye, X.; Fan, X.; Gao, C.; Quan, Y.; Wen, S.; Cai, X.; Huang, J.; Li, S. Insights into the improved cycle and rate performance by ex-situ F and in-situ Mg dual doping of layered oxide cathodes for sodium-ion batteries. *Energy Storage Mater.* **2022**, *45*, 1153–1164. [[CrossRef](#)]
36. Xie, Y.; Gabriel, E.; Fan, L.; Hwang, I.; Li, X.; Zhu, H.; Ren, Y.; Sun, C.; Pipkin, J.; Dustin, M.; et al. Role of Lithium Doping in P2-Na<sub>0.67</sub>Ni<sub>0.33</sub>Mn<sub>0.67</sub>O<sub>2</sub> for Sodium-Ion Batteries. *Chem. Mater.* **2021**, *33*, 4445–4455. [[CrossRef](#)]

37. Chen, C.; Huang, W.; Li, Y.; Zhang, M.; Nie, K.; Wang, J.; Zhao, W.; Qi, R.; Zuo, C.; Li, Z.; et al. P2/O3 biphasic Fe/Mn-based layered oxide cathode with ultrahigh capacity and great cyclability for sodium ion batteries. *Nano Energy* **2021**, *90*, 106504. [[CrossRef](#)]
38. Kang, K.; Meng, Y.S.; Bréger, J.; Grey, C.P.; Ceder, G. Electrodes with High Power and High Capacity for Rechargeable Lithium Batteries. *Science* **2006**, *311*, 977–980. [[CrossRef](#)]
39. Oku, M.; Tokuda, H.; Hirokawa, K. Final states after Ni 2p photoemission in the nickel—Oxygen system. *J. Electron Spectrosc. Relat. Phenom.* **1991**, *53*, 201–211. [[CrossRef](#)]
40. Moez, I.; Susanto, D.; Chang, W.; Lim, H.-D.; Chung, K.Y. Artificial cathode electrolyte interphase by functional additives toward long-life sodium-ion batteries. *Chem. Eng. J.* **2021**, *425*, 130547. [[CrossRef](#)]
41. Zuo, W.; Qiu, J.; Liu, X.; Ren, F.; Liu, H.; He, H.; Luo, C.; Li, J.; Ortiz, G.F.; Duan, H.; et al. The stability of P2-layered sodium transition metal oxides in ambient atmospheres. *Nat. Commun.* **2020**, *11*, 3544. [[CrossRef](#)] [[PubMed](#)]
42. Chen, X.; Jia, Z.; Lv, H.; Wang, C.; Zhao, N.; Guo, X. Improved stability against moisture and lithium metal by doping F into  $\text{Li}_3\text{InCl}_6$ . *J. Power Sources* **2022**, *545*, 231939. [[CrossRef](#)]
43. Zhang, L.; Guan, C.; Xie, Y.; Li, H.; Wang, A.; Chang, S.; Zheng, J.; Lai, Y.; Zhang, Z. Heteroatom-Substituted P2- $\text{Na}_{2/3}\text{Ni}_{1/4}\text{Mg}_{1/12}\text{Mn}_{2/3}\text{O}_2$  Cathode with {010} Exposing Facets Boost Anionic Activity and High-Rate Performance for Na-Ion Batteries. *ACS Appl. Mater. Interfaces* **2022**, *14*, 18313–18323. [[CrossRef](#)] [[PubMed](#)]
44. Qu, J.F.; Wang, W.; Chen, Y.; Li, G.; Li, X.G. Raman spectra study on nonstoichiometric compound  $\text{Na}_x\text{CoO}_2$ . *Phys. Rev. B* **2006**, *73*, 082518. [[CrossRef](#)]
45. Zhong, X.-B.; He, C.; Gao, F.; Tian, Z.-Q.; Li, J.-F. In situ Raman spectroscopy reveals the mechanism of titanium substitution in P2- $\text{Na}_{2/3}\text{Ni}_{1/3}\text{Mn}_{2/3}\text{O}_2$ : Cathode materials for sodium batteries. *J. Energy Chem.* **2021**, *53*, 323–328. [[CrossRef](#)]
46. Bao, S.; Huang, Y.-Y.; Wang, J.-Z.; Luo, S.-h.; Su, G.-Q.; Lu, J.-L. High-Operating Voltage, Long-Life Layered Oxides for Sodium Ion Batteries Enabled by Cosubstitution of Titanium and Magnesium. *ACS Sustain. Chem. Eng.* **2021**, *9*, 2534–2542. [[CrossRef](#)]
47. Tang, K.; Huang, Y.; Xie, X.; Cao, S.; Liu, L.; Liu, H.; Luo, Z.; Wang, Y.; Chang, B.; Shu, H.; et al. Electrochemical performance and structural stability of air-stable  $\text{Na}_{0.67}\text{Ni}_{0.33}\text{Mn}_{0.67-x}\text{Ti}_x\text{O}_2$  cathode materials for high-performance sodium-ion batteries. *Chem. Eng. J.* **2020**, *399*, 125725. [[CrossRef](#)]
48. Yang, L.; Li, X.; Liu, J.; Xiong, S.; Ma, X.; Liu, P.; Bai, J.; Xu, W.; Tang, Y.; Hu, Y.Y.; et al. Lithium-Doping Stabilized High-Performance P2- $\text{Na}_{0.66}\text{Li}_{0.18}\text{Fe}_{0.12}\text{Mn}_{0.7}\text{O}_2$  Cathode for Sodium Ion Batteries. *J. Am. Chem. Soc.* **2019**, *141*, 6680–6689. [[CrossRef](#)]
49. Wang, Q.; Mariyappan, S.; Rousse, G.; Morozov, A.V.; Porcheron, B.; Dedryvere, R.; Wu, J.; Yang, W.; Zhang, L.; Chakir, M.; et al. Unlocking anionic redox activity in O3-type sodium 3d layered oxides via Li substitution. *Nat. Mater.* **2021**, *20*, 353–361. [[CrossRef](#)] [[PubMed](#)]
50. Mao, Q.; Yu, Y.; Wang, J.; Zheng, L.; Wang, Z.; Qiu, Y.; Hao, Y.; Liu, X. Mitigating the P2-O2 transition and  $\text{Na}^+$ /vacancy ordering in  $\text{Na}_{2/3}\text{Ni}_{1/3}\text{Mn}_{2/3}\text{O}_2$  by anion/cation dual-doping for fast and stable  $\text{Na}^+$  insertion/extraction. *J. Mater. Chem. A* **2021**, *9*, 10803–10811. [[CrossRef](#)]
51. Li, L.; Su, G.; Lu, C.; Ma, X.; Ma, L.; Wang, H.; Cao, Z. Effect of lithium doping in P2-Type layered oxide cathodes on the electrochemical performances of Sodium-Ion batteries. *Chem. Eng. J.* **2022**, *446*, 136923. [[CrossRef](#)]
52. Buchholz, D.; Moretti, A.; Kloepsch, R.; Nowak, S.; Siozios, V.; Winter, M.; Passerini, S. Toward Na-ion Batteries—Synthesis and Characterization of a Novel High Capacity Na Ion Intercalation Material. *Chem. Mater.* **2013**, *25*, 142–148. [[CrossRef](#)]
53. Buchholz, D.; Chagas, L.G.; Vaalma, C.; Wu, L.; Passerini, S. Water sensitivity of layered P2/P3- $\text{Na}_x\text{Ni}_{0.22}\text{Co}_{0.11}\text{Mn}_{0.66}\text{O}_2$  cathode material. *J. Mater. Chem. A* **2014**, *2*, 13415–13421. [[CrossRef](#)]
54. Zheng, X.; Li, P.; Zhu, H.; Rui, K.; Zhao, G.; Shu, J.; Xu, X.; Sun, W.; Dou, S.X. New insights into understanding the exceptional electrochemical performance of P2-type manganese-based layered oxide cathode for sodium ion batteries. *Energy Storage Mater.* **2018**, *15*, 257–265. [[CrossRef](#)]
55. Peng, B.; Chen, Y.; Wang, F.; Sun, Z.; Zhao, L.; Zhang, X.; Wang, W.; Zhang, G. Unusual Site-Selective Doping in Layered Cathode Strengthens Electrostatic Cohesion of Alkali-Metal Layer for Practicable Sodium-Ion Full Cell. *Adv. Mater.* **2022**, *34*, 2103210. [[CrossRef](#)]
56. Venkateswara Rao, C.; Soler, J.; Katiyar, R.; Shojan, J.; West, W.C.; Katiyar, R.S. Investigations on Electrochemical Behavior and Structural Stability of  $\text{Li}_{1.2}\text{Mn}_{0.54}\text{Ni}_{0.13}\text{Co}_{0.13}\text{O}_2$  Lithium-Ion Cathodes via in-Situ and ex-Situ Raman Spectroscopy. *J. Phys. Chem. C* **2014**, *118*, 14133–14141. [[CrossRef](#)]
57. Yin, B.; Zhang, S.; Jiang, H.; Qu, F.; Wu, X. Phase-controlled synthesis of polymorphic  $\text{MnO}_2$  structures for electrochemical energy storage. *J. Mater. Chem. A* **2015**, *3*, 5722–5729. [[CrossRef](#)]
58. Dokko, K.; Mohamedi, M.; Anzue, N.; Itoh, T.; Uchida, I. In situ Raman spectroscopic studies of  $\text{LiNi}_x\text{Mn}_{2-x}\text{O}_4$  thin film cathode materials for lithium ion secondary batteries. *J. Mater. Chem.* **2002**, *12*, 3688–3693. [[CrossRef](#)]
59. Gao, S.; Zhan, X.; Cheng, Y.-T. Structural, electrochemical and Li-ion transport properties of Zr-modified  $\text{LiNi}_{0.8}\text{Co}_{0.1}\text{Mn}_{0.1}\text{O}_2$  positive electrode materials for Li-ion batteries. *J. Power Sources* **2019**, *410–411*, 45–52. [[CrossRef](#)]
60. Wang, S.Y.; Yan, M.Y.; Li, Y.; Vinado, C.; Yang, J.H. Separating electronic and ionic conductivity in mix-conducting layered lithium transition-metal oxides. *J. Power Sources* **2018**, *393*, 75–82. [[CrossRef](#)]
61. Song, S.; Kotobuki, M.; Zheng, F.; Xu, C.; Hu, N.; Lu, L.; Wang, Y.; Li, W.-D. Y-Doped  $\text{Na}_2\text{ZrO}_3$ : A Na-Rich Layered Oxide as a High-Capacity Cathode Material for Sodium-Ion Batteries. *ACS Sustain. Chem. Eng.* **2017**, *5*, 4785–4792. [[CrossRef](#)]

62. Zhan, X.; Lai, S.; Gobet, M.P.; Greenbaum, S.G.; Shirpour, M. Defect chemistry and electrical properties of garnet-type  $\text{Li}_7\text{La}_3\text{Zr}_2\text{O}_{12}$ . *Phys. Chem. Chem. Phys.* **2018**, *20*, 1447–1459. [[CrossRef](#)]
63. Paulsen, J.M.; Dahn, J.R. Studies of the layered manganese bronzes,  $\text{Na}_{2/3}[\text{Mn}_{1-x}\text{M}_x]\text{O}_2$  with  $\text{M}=\text{Co}$ ,  $\text{Ni}$ ,  $\text{Li}$ , and  $\text{Li}_{2/3}[\text{Mn}_{1-x}\text{M}_x]\text{O}_2$  prepared by ion-exchange. *Solid State Ion.* **1999**, *126*, 3–24. [[CrossRef](#)]
64. Li, R.; Jiang, D.; Du, P.; Yuan, C.; Cui, X.; Tang, Q.; Zheng, J.; Li, Y.; Lu, K.; Ren, X.; et al. Negating  $\text{Na}||\text{Na}_3\text{Zr}_2\text{Si}_2\text{PO}_{12}$  interfacial resistance for dendrite-free and “Na-less” solid-state batteries. *Chem. Sci.* **2022**, *13*, 14132–14140. [[CrossRef](#)] [[PubMed](#)]
65. Talyosef, Y.; Markovsky, B.; Salitra, G.; Aurbach, D.; Kim, H.J.; Choi, S. The study of  $\text{LiNi}_{0.5}\text{Mn}_{1.5}\text{O}_4$  5-V cathodes for Li-ion batteries. *J. Power Sources* **2005**, *146*, 664–669. [[CrossRef](#)]

**Disclaimer/Publisher’s Note:** The statements, opinions and data contained in all publications are solely those of the individual author(s) and contributor(s) and not of MDPI and/or the editor(s). MDPI and/or the editor(s) disclaim responsibility for any injury to people or property resulting from any ideas, methods, instructions or products referred to in the content.